Correlation-based dip-guided optimal stacking

Lorenzo Casasanta and Sergio Grion, Shearwater Geoservices

Copyright 2023, SBGf - Sociedade Brasileira de Geofísica

This paper was prepared for presentation during the 18th International Congress of the Brazilian Geophysical Society held in Rio de Janeiro, Brazil, 16-19 October 2023.

Contents of this paper were reviewed by the Technical Committee of the 18th International Congress of the Brazilian Geophysical Society and do not necessarily represent any position of the SBGf, its officers or members. Electronic reproduction or storage of any part of this paper for commercial purposes without the written consent of the Brazilian Geophysical Society is prohibited.

Abstract

Optimizing the stacking weights of prestack volumes can improve the stacked image. However, existing optimal stacking methods either are not effective in the presence of event misalignments or require complex a-priori dip computations. Our correlation-based dip-guided optimal stacking overcomes these limitations by measuring the dip coherency of each prestack volume by computing the local correlation between filtered images of that individual gather. It can be efficiently implemented using simple 2D plane-wave destruction filters (PWD) and a sliding-window correlation. Our synthetic example shows that this method provides comparable or slightly better results than a dip-guided method that pre-computes the dip of prestack volumes.

Introduction

Prestack volumes are image volumes sorted by shot patches, reflection angles/azimuths, vector offsets or other seismic attributes. Stacking the prestack volumes is an important step to improve the signal-to-noise ratio and the image quality of seismic data. The basic idea of optimal stacking is to optimize the stacking weights to emphasize the relevant structural information in prestack volumes while down weighting or removing noise or artifacts.

Many optimal stacking methods are based on local correlation. Grion and Mazzotti (1998) compare weights estimated using cross-correlation and singular value decomposition and conclude that the former performs equally well to the latter but has reduced computational cost. Liu et al. (2009) use as stacking weights the local correlation coefficients between each trace in the prestack volumes and a reference trace from a conventional stacked image. Sanchis and Hanssen (2012) propose to improve the correlation results using preprocessed reference traces. Compton and Stork (2012) further improve the technique with more spatial information by incorporating a 3D cube of prestack traces and reference traces when calculating local correlations. However, it is expected that local correlation does not perform well if events from different prestack volumes are not perfectly aligned due to velocity errors.

Using an interpreted reference dip field to guide the stacking should theoretically mitigate this issue. Dip-guided optimal stacking assigns more weight to prestack events with dips that better conform the interpreted reference 3D dip, while down-weighting or excluding events that do not. The reference dip field could come from a heavily pre-processed reference stack, interpreted horizons or other geological information. One drawback of existing dip-guided optimal stacking methods is that they either require difficult computations of dip fields from prestack volumes (Gu et al., 2016; Malave et al., 2017), or they require that the dip-guided stacking be limited to dip gathers (Hartman et al., 2015).

We propose a method to perform dip-guided optimal stacking based on using correlations to measure dip coherency. It combines the merits of the local correlation and the guided-dip methods while avoiding their limitations. Our method measures dip coherency of a gather using local correlations between a set of dip-filtered versions of the gather itself. Despite its simplicity, this methodology has a solid theoretical basis that we will discuss in the next section.

Method

For convenience we here consider the case of a 2D image $I(z,x)$. The simplest dip filter is the plane-wave destruction filter (PWD) (Claerbout, 1992; Fomel, 2002)

$$PWD(I,\sigma) = \frac{\partial I}{\partial x} + \sigma \frac{\partial I}{\partial z} \qquad (1)$$

where $I(z,x)$ is a prestack image and $\sigma = \tan(\theta)$ is the reference local slope as a function of local dip θ. Examples of reference slope σ and image I are shown in Figure 1a and 1b, respectively.

For convenience, we define

$$PWDsin(I,\sigma) = \frac{\frac{\partial I}{\partial x} + \sigma \frac{\partial I}{\partial z}}{\sqrt{1+\sigma^2}} \approx \sin(\Delta\theta)\nabla_{\mathbf{n}} I \qquad (2)$$

and

$$PWDcos(I,\sigma) = \frac{-\sigma \frac{\partial I}{\partial x} + \frac{\partial I}{\partial z}}{\sqrt{1+\sigma^2}} \approx \cos(\Delta\theta)\nabla_{\mathbf{n}} I \qquad (3)$$

where $PWDsin$ is a normalized version of PWD and $PWDcos$ represents the application of PWD along a direction perpendicular to the reference dip. The right-hand sides of equations (2) and (3) are derived assuming a local reflection plane with dip θ_I in I, and $\Delta\theta = \theta - \theta_I$. $\nabla_{\mathbf{n}} I$ is a

directional derivative taken in the direction normal to this local reflection plane.

More intuitive explanations for the modified $PWDsin$ and $PWDcos$ are shown in Figure 1c and 1d, respectively. We can observe that $PWDsin$ kills events that conform to the reference dip, whereas $PWDcos$ kills those orthogonal to it.

We use these PWD filtered images to compute the stacking weights. We do not dip filter any events in the final optimized stacked image. The following section describes how we use a local correlation measure to extract the dip coherency from the PWD filtered images.

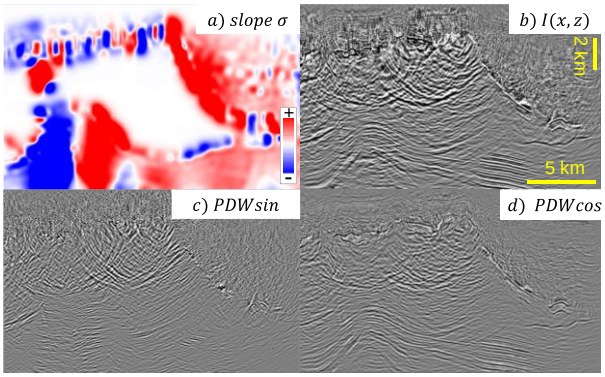

Figure 1: An example of (a) reference slope σ, (b) image I, (c) $PWDsin$ filtered image, (d) $PWDcos$ filtered image.

Workflow

In 3D, we use reference local slopes/dips $\sigma_x = \tan\theta_x$ and $\sigma_y = \tan\theta_y$ along the crossline and inline directions, respectively, to guide the stacking. There are three main steps for measuring the dip coherency using our method:

1) For each individual 3D image I, compute four 3D PWD filtered images:

$$PWDsin(I,\sigma_x), PWDcos(I,\sigma_x),$$
$$PWDsin(I,\sigma_y), PWDcos(I,\sigma_x). \quad (4)$$

The PWD filtered images in equation (4) are obtained by applying our 2D modified PWDs to all the 2D planes along crossline and inline directions, respectively.

2) Apply the local correlation operator $\langle , \rangle$, to combinations of PWD filtered images in equation (4), namely

$$c_1 = \langle PWDcos(I,\sigma_x), PWDcos(I,\sigma_y)\rangle$$
$$c_2 = \langle PWDcos(I,\sigma_x), PWDsin(I,\sigma_y)\rangle$$
$$c_3 = \langle PWDsin(I,\sigma_x), PWDcos(I,\sigma_y)\rangle \quad (5)$$
$$c_4 = \langle PWDsin(I,\sigma_x), PWDsin(I,\sigma_y)\rangle$$

Where $C(z,y,x) = \langle I_1(z,y,x), I_2(z,y,x)\rangle$ and its discretized version is

$$c(i_x,i_y,i_z) = \sum_{j_x=-w_x}^{j_x=w_x}\sum_{j_y=-w_y}^{j_y=w_y}\sum_{j_z=-w_z}^{j_z=w_z} f(j_x,j_y,j_z) I_1(i_x,i_y,i_z) I_2(i_x,i_y,i_z) \quad (6)$$

Here, $f(j_x,j_y,j_z)$ is the weighting function for 3D window summation and w_x, w_y, w_z are the windows half-lengths in number of samples. If the weight is constant, local correlation is implemented using sliding-window correlation (Liu et al., 2009; Sanchis and Hanssen, 2012).

3) Define $\Delta\theta_{3D}$ as the angle between the normal directions of a local reflection plane in the 3D image I and the local plane defined by the reference crossline and inline dips. We compute $\cos(\Delta\theta_{3D})$ at every sample following the formula.

$$\cos(\Delta\theta_{3D}) = \frac{X + \sigma_x Y + \sigma_y Z}{\sqrt{X^2+Y^2+Z^2}\sqrt{1+\sigma_x^2+\sigma_y^2}} \quad (7)$$

Where X, Y and Z are linear combinations of the four local correlations from equation (6):

$$X = c_1 + \sigma_y c_2 + \sigma_x c_3 + \sigma_x\sigma_y c_4$$
$$Y = \sigma_x c_1 + \sigma_x\sigma_y c_2 - c_3 - \sigma_y c_4 \quad (8)$$
$$Z = \sigma_y c_1 - c_2 + \sigma_x\sigma_y c_3 - \sigma_x c_4$$

Appendix B shows the derivation of equations (4) to (8).

The above three steps are applied individually to each prestack gather to estimate dip coherency $\cos^2(\Delta\theta_{3D})$, which has a value between 0 and 1. A value of 1 indicates that the prestack volume sample completely conforms to the reference dip, while a value of 0 indicates that the sample completely disagrees with the reference dip. This dip coherency is used as stacking weight after thresholding.

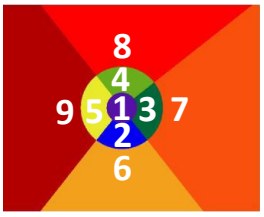

Figure 2: Aperture volume decomposition. The inner sector 1 has a radius of 1km. The 8 outer sectors have azimuth of 45, 135, 225, 315 degrees with sectors 2,3,4,5 extending between 1km and 2.6km. The remaining sectors extend beyond 2.6km to the rest of the aperture domain.

Examples

We apply this method to RTM images generated from the 3D SEAM model. The simulated acquisition is off-end streamer. A total of 57 sail line data have been simulated using a sparse shot grid with 150m inline and 600m crossline shot-spacing. The simulation uses 20 streamer cables spaced 60m apart with a receiver spacing of 30m. The streamers are symmetric around the shot line with a maximum inline offset of ± 570m. The simulated acquisition direction is E-W with a maximum positive crossline offset of 8.2km.

Each RTM shot image uses an operator with 8km inline aperture and 6km crossline aperture. The migrated shots are decomposed into nine partitions as a function of the aperture offset and azimuth as shown in the graph in Figure 2. Each numbered sector in Figure 2 corresponds to a pre-stack volume in Figure 3

The conventional straight stack image in Figures 4a (crossline slice) and 5a (depth slice) shows that the subsalt image pointed by the yellow arrow is much distorted.

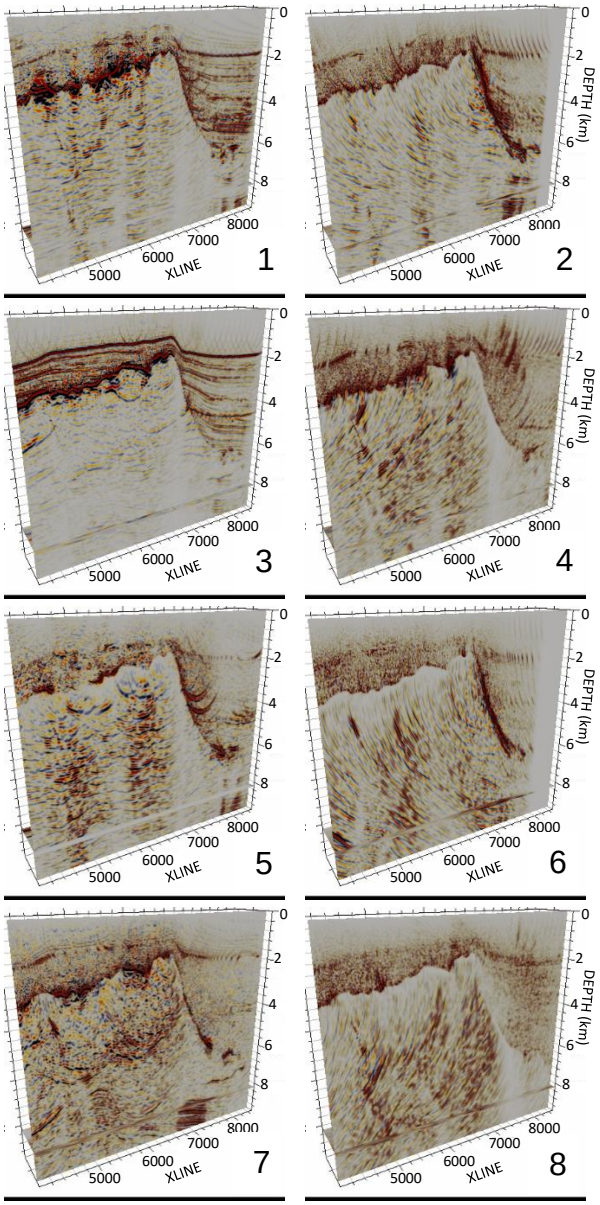

Figure 3: Eight of the nine 3D RTM prestack volumes decomposed based on offset and azimuth aperture as described in Figure 2. With an E-W acquisition direction we expect little or no image from large negative crossline offsets. This is confirmed by inspecting sector 9, which contains no useful structural information, and therefore it is not shown here.

We compare our correlation-based dip-guided optimal stacking method to a conventional dip- consistency method which requires a-priori computation of the prestack dip. For convenience, we use a reference dip field directly computed from the true reflectivity model. Both methods significantly improve the final stack image as shown in Figures 4 and 5 for crossline and depth slices, respectively. Our method provides comparable subsalt image quality to the conventional method at the yellow arrow location. In addition, our method removes or attenuates strong false coherent events at the blue arrow locations, which do not appear in the true model. Our method also improves the continuity at the red arrow location, while the conventional method makes it worse.

For validation, in Figure 6 we compare coherency $cos^2(\Delta\theta_{3D})$ maps at the location of the 2D slices in Figure 1 using conventional dip-consistency methodology and our novel dip-coherency approach. Without computing the dip field of the prestack volume, our method can provide comparable measurement of dip coherency compared to more traditional approaches.

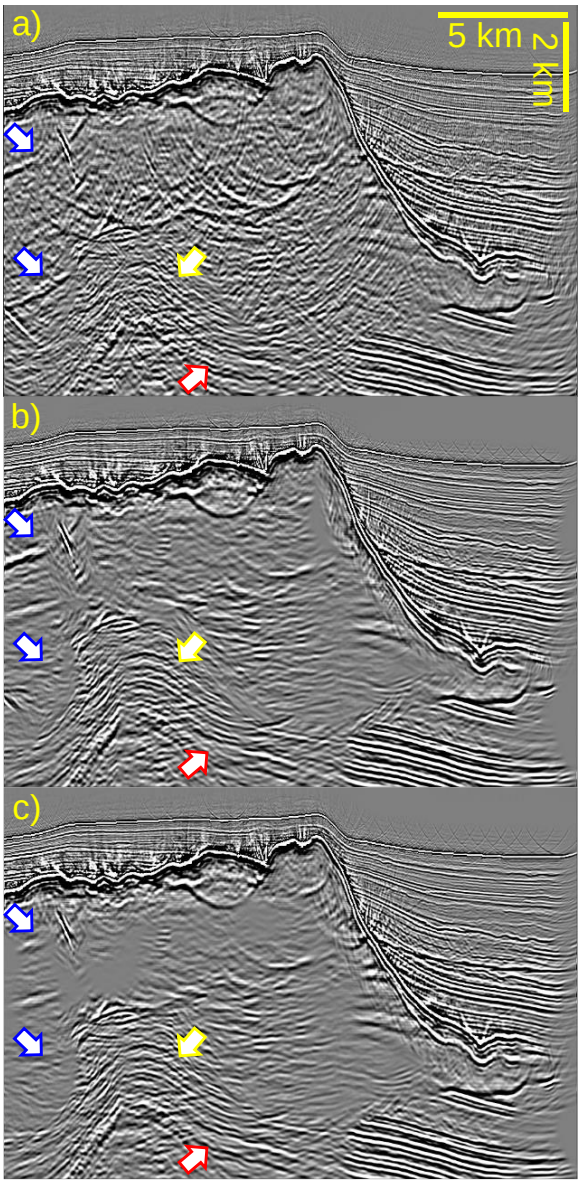

Figure 4: Crossline slice of (a) straight stack image, (b) conventional and (c) correlatino-based dip-guided optimal stack.

Conclusions

We introduce the correlation-based dip-guided optimal stacking method. The method does not require the computation of prestack dip fields. It also assesses coherency within individual gathers, therefore overcoming the local correlation issue with event misalignments in the gathers due to velocity errors. Our synthetic example shows that even when applied using simple 2D PWDs and sliding window correlations, our method provides comparable or slightly improved results with respect to conventional dip-guided methods.

Acknowledgments

The authors are in debt to Zongcai Feng, who formulated the dip coherency measure and implemented it as a by-product of conventional PWD wave killers.

References

Claerbout, J.F. and Abma, R., 1992. Earth soundings analysis: Processing versus inversion (Vol. 6). London: Blackwell Scientific Publications.

Compton, S. and Stork, C., 2012, November. 3D nonlinear stack enhancement: Correlation based stacking. In 2012 SEG Annual Meeting. OnePetro.

Fomel, S., 2002. Applications of plane-wave destruction filters. Geophysics, 67(6), pp.1946-1960.

Grion, S., Mazzotti, A., 1998, Stacking weights determination by means of SVD and cross-correlation. In SEG Technical Program Expanded Abstracts 1998 (pp. 1135-1138). Society of Exploration Geophysicists.

Gu, R., Zdraveva, O., Hegazy, M. and Buzzell, S., 2016. Interpretation-guided image enhancement using reverse-time-migration vector-image partitions. In SEG Technical Program Expanded Abstracts 2016 (pp. 4341-4345). Society of Exploration Geophysicists.

Hartman, K., Chakraborty, S., Nolte, B., Gou, W., Sun, Q. and Chazalnoel, N., 2015. Understanding and improving the subsalt image at Thunder Horse, Gulf of Mexico. In SEG Technical Program Expanded Abstracts 2015 (pp. 4028-4032). Society of Exploration Geophysicists.

Liu, G., Fomel, S., Jin, L. and Chen, X., 2009. Stacking seismic data using local correlation. Geophysics, 74(3), pp. V43-V48.

Malave, K., Hegazy, M., Hydal, S., Jones, L. and Tu, C., 2017. Enhanced imaging using targeted reprocessing: A Gulf of Mexico case study. In SEG Technical Program Expanded Abstracts 2017 (pp. 5756-5760). Society of Exploration Geophysicists.

Sanchis, C. and Hanssen, A., 2011. Enhanced local correlation stacking method. Geophysics, 76(3), pp. V33-V45.

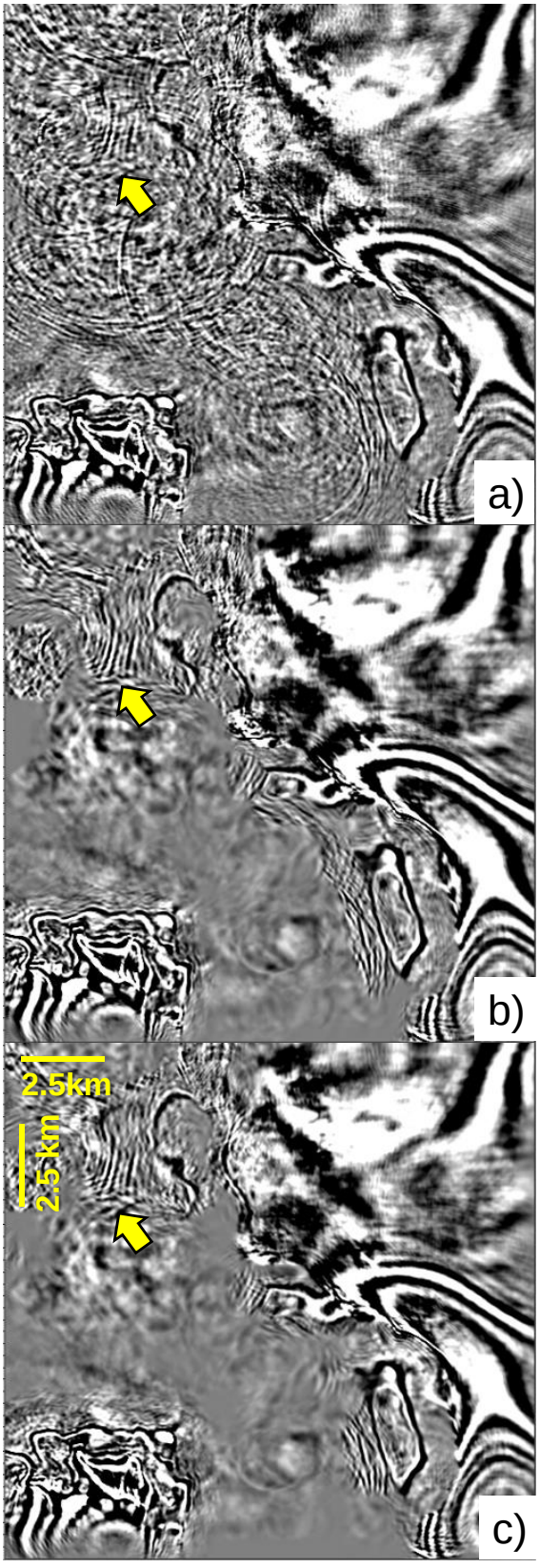

Figure 5: Depth slice of (a) a stacked image, (b) the corresponding conventional and (c) correlatio-based dip-guided optimal stack.

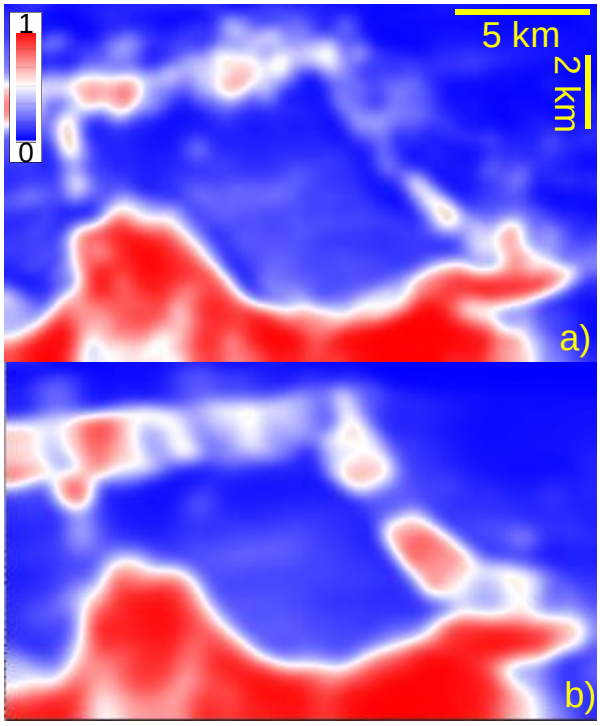

Figure 6: Dip coherency using (a) conventional and (b) correlation-based dip-guided method

Appendix A

Following the notation introduced in Figure 7, we define

$$\frac{\partial I}{\partial x} \approx -\sin(\theta')\nabla_{\mathbf{n}} I, \quad \frac{\partial I}{\partial z} \approx \cos(\theta')\nabla_{\mathbf{n}} I \qquad (9)$$

Substituting equation (A1) and $\sigma = \tan(\theta)$ into equations (2) and (3) yields

$$\begin{aligned} PWDsin(I,\sigma) &= \left(\frac{\partial I}{\partial x} + \sigma\frac{\partial I}{\partial z}\right) / \sqrt{1+\sigma^2} \\ &\approx -\cos(\theta)\sin(\theta')\nabla_{\mathbf{n}} I + \sin(\theta)\cos(\theta')\nabla_{\mathbf{n}} I \\ &\approx \sin(\theta-\theta')\nabla_{\mathbf{n}} I \end{aligned} \qquad (10)$$

and

$$\begin{aligned} PWDcos(I,\sigma) &= \left(-\sigma^2\frac{\partial I}{\partial x} + \frac{\partial I}{\partial z}\right) / \sqrt{1+\sigma^2} \\ &\approx \sin(\theta)\sin(\theta')\nabla_{\mathbf{n}} I + \cos(\theta)\cos(\theta')\nabla_{\mathbf{n}} I \\ &\approx \sin(\theta-\theta')\nabla_{\mathbf{n}} I \end{aligned} \qquad (11)$$

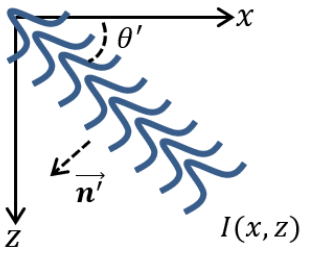

Figure 7: Notation of local dip θ' and normal direction $\mathbf{n}'$ of a local reflection plane in image $I(x,z)$.

Appendix B

We denote the 3D normal direction of reference plane as $\mathbf{n} = \begin{pmatrix} n_x & n_y & n_z \end{pmatrix}$. According to the definition of crossline and inline dips σ_x and σ_y, we have

$$\mathbf{n}\cdot\begin{pmatrix}\sigma_x & 0 & 1\end{pmatrix} = 0 \text{ and } \mathbf{n}\cdot\begin{pmatrix}0 & \sigma_y & 1\end{pmatrix} = 0 \qquad (B1)$$

Solving for $\mathbf{n}$ which gives

$$\mathbf{n} = \left(-\frac{1}{S} \quad \frac{\sigma_x}{S} \quad \frac{\sigma_y}{S}\right) \qquad (12)$$

where $S = \sqrt{1+\sigma_x^2+\sigma_y^2}$. For the image I, we denote its local slopes as $\sigma_x' = \tan(\theta_x')$ and $\sigma_y' = \tan(\theta_y')$ along the crossline and inline directions, respectively. Its normal direction is

$$\mathbf{n} = \left(-\frac{1}{S'} \quad \frac{\sigma_x'}{S'} \quad \frac{\sigma_y'}{S'}\right) \qquad (13)$$

where $S' = \sqrt{1+(\sigma_x')^2+(\sigma_y')^2}$. Thus $\cos(\Delta\theta_{3D})$ can be computed as

$$\begin{aligned} \cos(\Delta\theta_{3D}) &= \mathbf{n}'\cdot\mathbf{n} = \frac{1+\sigma_x'\sigma_x+\sigma_y'\sigma_y}{S'S} \\ &= \frac{\cos\theta_x'\cos\theta_y' + \cos\theta_y'\sin\theta_x'\sigma_x + \cos\theta_x'\sin\theta_y'\sigma_y}{S\sqrt{\left(\cos\theta_x'\cos\theta_y'\right)^2+\left(\cos\theta_y'\sin\theta_x'\right)^2+\left(\cos\theta_x'\sin\theta_y'\right)^2}} \end{aligned} \qquad (14)$$

Using the identity

$$\frac{\cos\theta_x'}{\cos\theta_x} = \frac{\cos(\theta_x-\Delta\theta_x)}{\cos\theta_x} = \cos\Delta\theta_x + \sigma_x\sin\Delta\theta_x \qquad (15)$$

we define

$$A = PWDcos(I,\sigma_x) + \sigma_x PWDsin(I,\sigma_x) \qquad (16)$$

Similarly, we also define

$$\begin{aligned} B &= PWDcos(I,\sigma_y) + \sigma_y PWDsin(I,\sigma_y) \\ C &= \sigma_x PWDcos(I,\sigma_x) - PWDsin(I,\sigma_x) \\ D &= \sigma_y PWDcos(I,\sigma_x) - PWDsin(I,\sigma_y) \end{aligned} \qquad (17)$$

Finally, equation B4 reduces to

$$\cos(\Delta\theta_{3D}) \approx \frac{\langle A,B\rangle + \langle B,C\rangle\sigma_x + \langle A,D\rangle\sigma_y}{S\sqrt{\langle A,B\rangle^2 + \langle B,C\rangle^2 + \langle A,D\rangle^2}} \qquad (18)$$

Comparing equations 7 and B10, we note that

$$X = \langle A,B\rangle, \quad Y = \langle B,C\rangle, \quad Z = \langle A,D\rangle \qquad (19)$$

The difference between equations 7 and B8 is that equation B8 first computes the linear combinations of PWD filtered images followed by local correlations, while equation 7 computes local correlations followed by linear combinations. For reason of convenience our implementation is based on equation B8.